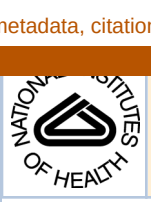

Published in final edited form as:

Langmuir. 2012 June 19; 28(24): 9131–9139. doi:10.1021/la3005213.

In situ measurement of bovine serum albumin interaction with gold nanospheres

Sergio Dominguez-Medina[1], **Steven McDonough**[1], **Pattanawit Swanglap**[1], **Christy F. Landes**[1], and **Stephan Link**[1,2,*]

[1]Department of Chemistry, Laboratory for Nanophotonics, Rice University, Houston, Texas 77005

[2]Department of Electrical and Computer Engineering, Laboratory for Nanophotonics, Rice University, Houston, Texas 77005

Abstract

Here we present *in situ* observations of adsorption of bovine serum albumin (BSA) on citrate-stabilized gold nanospheres. We implemented scattering correlation spectroscopy as a tool to quantify changes in the nanoparticle Brownian motion resulting from BSA adsorption onto the nanoparticle surface. Protein binding was observed as an increase in the nanoparticle hydrodynamic radius. Our results indicate the formation of a protein monolayer at similar albumin concentrations as those found in human blood. Additionally, by monitoring the frequency and intensity of individual scattering events caused by single gold nanoparticles passing the observation volume, we found that BSA did not induce colloidal aggregation, a relevant result from the toxicological viewpoint. Moreover, to elucidate the thermodynamics of the gold nanoparticle-BSA association, we measured an adsorption isotherm which was best described by an anti-cooperative binding model. The number of binding sites based on this model was consistent with a BSA monolayer in its native state. In contrast, experiments using poly-ethylene glycol capped gold nanoparticles revealed no evidence for adsorption of BSA.

Keywords

Gold nanoparticles; surface plasmon; bovine serum albumin; protein corona; correlation spectroscopy; diffusion

1. Introduction

The safe use of nanoparticles in *in vivo* applications requires a clear understanding of the nanoparticle interface.[1–3] How nanoparticles diffuse and interact with biomolecules in complex biological fluids is an intriguing question that receives growing attention.[4–6] For instance, the interaction of nanoparticles with blood plasma is of special interest[7–9] because many of their intended biomedical applications (e.g. drug delivery,[10–12] disease diagnosis and treatment[13–17]) often require an intravenous approach.

*Corresponding author, slink@rice.edu.

Supporting Information Available.

Size distributions of the samples used obtained via TEM images, UV/Vis extinction spectra of 70 and 93 nm AuNPs, error analysis and determination of the focal volume in scattering correlation spectroscopy experiments, intensity transient and autocorrelation curve of pure BSA solutions, effect of τ_{max} and the number of events on the retrieved value of R_h, the distribution of R_h for 70 and 93 nm AuNPs, an individual 40 s scattering intensity transient with its corresponding autocorrelation curve, and Zeta-potential measurements on 51 nm citrate-capped and 56 nm PEG-coated AuNPs before and after interaction with BSA. This material is available free of charge via the Internet at http://pubs.acs.org.

Recent studies have demonstrated that once nanoparticles are introduced into plasma they can become coated by the vast collection of biomolecules present in this medium, forming a 'corona' that surrounds the nanoparticles and shields their original surface properties.[18–20] Serum proteins play a major role in these interactions because they constitute the majority of the plasma fluid and have comparable nano-scale sizes.[21] It is thought that the affinity of a certain protein to bind to a nanoparticle surface is determined by the nanoparticle size,[22,23] shape,[24] and surface chemistry.[22,24]

The role of a corona masking the designed surface chemistry of nanoparticles is a critical issue as cellular uptake and its associated physiological response are regulated by chemical interactions at the nanoparticle surface.[21,25] Doorley *et al.*[26] demonstrated the co-localization of 200 nm polysterene beads and serum albumin, the most abundant protein in human blood,[27] at the membrane of kidney cells. This has the subtle yet critical implication that what the cell actually 'sees' is not the nanoparticle core or the initially synthesized organic interface but the bound proteins forming a corona on the nanoparticle surface. A recent report by Deng *et al.* [28] showed how 5 and 20 nm poly-acrylic acid coated gold nanoparticles bound to and induced unfolding of fibrinogen, thereby exposing a specific amino acid combination that interacts with an important receptor on human leukemia cells causing the release of cytokines and hence inflammation. Such protein-nanoparticle hybrids could show long term stability under *in vivo* conditions and trigger undesired signals in cellular receptors that would otherwise remain inactive. The necessary knowledge of these unwanted side effects encourages fundamental research on the characterization of the nanoparticle interface when exposed to physiological environments.

Nanoparticle-protein associations have been characterized by several different methods that typically require the separation of the nanoparticles from the adsorbed proteins, followed by the identification of the isolated organic compounds.[29] A common approach involves isolation via size exclusion chromatography or differential centrifugation, followed by protein identification via gel electrophoresis and mass spectrometry.[30] Deposition of a dried sample on a substrate has been useful for structural imaging via transmission electron microscopy, while the identification of the protein corona is done by staining of the organic compounds.[8] Most strategies therefore involve the removal of the nanoparticle-protein complexes from their original physiological environments.[21]

A complimentary *in situ* approach to these previous studies measures diffusion parameters before and after protein adsorption.[31] This allows one to address such important issues as the amount of adsorbed protein and the fate of the nanoparticle-protein complexes directly in physiological environments. The latter is especially critical from a toxicological viewpoint if adsorbed proteins induce nanoparticle aggregation,[32] which may complicate cellular uptake and clearance, or if nanoparticles induce protein aggregation,[33] which is often associated with a variety of diseases. Therefore, *in situ* observations of protein adsorption on nanoparticles under physiological conditions are required for the safe development of the emerging field of nanomedicine.

Gold nanoparticles (AuNPs) have emerged as a favorable platform for potential applications in nanomedicine because of the established non-toxicity of the gold core.[34] Furthermore AuNPs are attractive because their strong plasmon resonance makes it possible to simultaneously use them as optical probes.[35–37] However, *in situ* characterization of AuNPs interacting with proteins are scarce and, to some extent, contradicting as both monolayer[19,31] and multilayer[20,24] adsorption of serum albumin have been reported for AuNPs in a physiological environment. Additionally, disagreement exists in the literature on whether BSA stabilizes the NP colloid[19,31,38] or induces NP aggregation[20,24]. The mechanism for BSA adsorption on negatively charged citrate-stabilized AuNPs is also under

debate. Both an electrostatic attraction via the positively charged lysine groups of BSA[19,38] and a ligand exchange reaction with the sulfur of the cysteine residue that binds to the AuNP surface[31] have been suggested. Because nanoparticle-protein interactions and the possible formation of a protein corona are thought to depend on many parameters including nanoparticle size and shape as well as surface chemistry, further quantitative *in situ* measurements are necessary.

Here, we use plasmon scattering correlation spectroscopy[39] to explore *in situ* protein adsorption on AuNPs by monitoring the changes in the Brownian diffusion due to protein binding. Bovine serum albumin (BSA) was used a model protein and shares almost identical structure, function, and pH-dependent transitions with its human counterpart.[27,40] Our results indicate the formation of a BSA monolayer at blood plasma concentrations on citrate-stabilized AuNPs independent of AuNP size in the range of 51 – 93 nm. Citrate-stabilized AuNPs were used because they are the most common spherical AuNPs used. Burst intensity frequency analysis (BIFA)[41] of scattering transients furthermore reveals that BSA adsorption does not induce colloid aggregation for these AuNPs. Based on the results of an adsorption isotherm, we demonstrate that BSA adsorption occurs spontaneously via an anti-cooperative binding mechanism. Finally, experiments with poly-ethylene glycol (PEG) functionalized AuNPs show that the PEG coating provides protection from BSA adsorption.

2. Experimental Section

2.1 Materials

Citrate-stabilized AuNPs with three distinct diameters (51, 70, and 93 nm) and 56 nm AuNPs capped with PEG (M_W = 5,000) were purchased from Nanopartz Inc. BSA (≥98% lyophilized powder, M_W = 66,430) was obtained from Sigma-Aldrich Corp. The purity of the protein was comparable to previous nanoparticle studies.[18–20,24,31,38] Contamination by small molecules can be neglected as they do not cause a measurable effect in the correlation spectroscopy measurements. The protein powder was suspended and diluted to the desired concentration (0.75 mM unless noted otherwise) in 25 mM 4-(2-hydroxyethyl)-1-piperazineethanesulfonic acid (HEPES buffer, Life Technologies™), 20 mM NaCl (Sigma-Aldrich) and Ultrapure™ molecular biology grade water (Gibco). The BSA solutions were freshly prepared for each experiment, or otherwise stored at −20 °C to reduce protein aggregation and sedimentation. The pH of this solution was in the physiological range (7.0 – 7.5). The AuNPs were also diluted in this buffer to picomolar concentrations (~10^{10} particles/mL). For protein binding experiments, AuNP and BSA solutions were mixed using equal volumes and then measured immediately. Microscope cover glass slides (25 × 25 mm^2, Fisherbrand) were sonicated in acetone (ACS spectrophotometric grade, Sigma-Aldrich), 1% Liquinox™ (Alconox Inc.), and Milli DI™ water (>25 MΩ, Millipore) followed by drying with ultra high purity N_2 (Matheson) and O_2 plasma cleaning for 1 minute at 300 mTorr (Harrick Plasma). To avoid unwanted protein adsorption to the substrate, the cover glass was treated with Vectabond reagent (Vector Labs) and PEG-5000 (Sigma-Aldrich) following a procedure described elsewhere.[42] Silicon chambers (50 μL, Grace Bio-Labs) were placed on top of the microscope coverslips and filled with the solution of interest.

2.2 AuNP Characterization

The AuNPs were characterized using transmission electron microscopy (TEM, JEOL 2010) and ensemble UV/Vis spectroscopy (Ocean Optics) as shown in Figure 1 and in the supporting information (Figures S1 and S2). The size distribution of each sample was obtained from the TEM images using an automated Matlab program. Two perpendicular axes were measured per AuNP and the results are summarized in Table S1. The AuNPs were mostly spherical as indicated by the black dashed lines in Figures 1A and S1. Zeta

potentials were measured for AuNPs only and AuNPs with BSA added using a Malvern Zen 3600 (Zetasizer Nano). The samples were prepared in the same way as described above. The Smoluchowski approximation (F(Ka) = 1.5) was used as an input parameter of the Henry equation, corresponding to the electrophoretic mobility of small particles in aqueous media.

2.3 Optical Setup for Scattering Correlation Spectroscopy

Scattering correlation spectroscopy was performed using a home-built inverted confocal microscope (Observer. D1, Zeiss). Briefly, light from a 532 nm laser (Verdi-6, Coherent Inc.) was collimated and expanded to overfill the back aperture of a microscope objective (Fluar, Zeiss: 100X, N.A. = 1.3). The beam was circularly polarized using a λ/4 waveplate (Newport). The laser power was attenuated to ~ 150 nW using neutral density filters (Thorlabs). This power gave a signal to background ratio of ~ 10, yet ensured negligible heating of the sample.[39] The focal plane of the objective was set to approximately ~ 6 μm inside the solution to avoid excessive scattered light from the glass-water interface. Orange fluorescent polystyrene beads (100 nm in diameter, Molecular Probes®) were used for alignment and calibration of the focal volume (Figure S3). AuNPs diffusing across this diffraction limited focal volume scattered light due to their inherent surface plasmon resonance. Plasmon scattering was chosen for these experiments instead of one-photon plasmon luminescence of the AuNPs[39] because of an interfering background signal from auto-fluorescence by the BSA solution. For the scattering geometry, fluorescence was negligible at the excitation powers used (Figure S4). The scattered light was collected in the backwards direction and redirected to a 50 μm pinhole (Thorlabs) before focusing onto an avalanche photodetector (SPCM-AQRH, Perkin Elmer).

2.4 Analysis of Scattering Correlation Spectroscopy

Correlation spectroscopy yields the characteristic diffusion time τ_D of an analyte of interest as it diffuses through a diffraction limited focal volume. Due to the low concentrations used (typically < nM), it is assumed that only one analyte crossed the focal volume (< 1 fL) at a time. Fluctuations in the scattering intensity $I(t)$ were observed when AuNPs were optically excited while diffusing across this focal volume. Temporal autocorrelation analysis of the scattering signal was performed over a range of lag times τ from τ_{min} to τ_{max}:[43]

$$G(\tau)=\frac{\langle \delta I(t)\cdot \delta I(t+\tau)\rangle}{\langle I(t)\rangle^2} \quad (1)$$

Here $G(\tau)$ represents the autocorrelation function and $\delta I(t)$ an intensity fluctuation, which is mathematically represented as the signal at time t minus the average: $\delta I(t) = I(t) - \langle I(t)\rangle$. For the case of a Gaussian excitation profile, Aragon *et al.*[44] derived the three dimensional autocorrelation function in terms of the average number of species crossing the focal volume $\langle N\rangle$, the beam waist r_0, and beam height z_0:

$$G(\tau)=\frac{1}{\langle N\rangle}\cdot\frac{1}{\left(1+\frac{\tau}{\tau_D}\right)}\cdot\frac{1}{\left(1+\left(\frac{r_0}{z_0}\right)^2\left(\frac{\tau}{\tau_D}\right)\right)^{1/2}} \quad (2)$$

The experimental autocorrelation was fitted to equation (2), where τ_D and $\left(\frac{r_0}{z_0}\right)$ were used as fit parameters. The amplitude was normalized for better comparison of the differences in τ_D associated with BSA binding. The characteristic diffusion time is related to the translational diffusion coefficient D_{tr} by the following relationship:[43]

$$\tau_D = \frac{r_0^2}{4D_{tr}} \quad (3)$$

The Stokes-Einstein equation then yields the hydrodynamic radius R_h:

$$D_{tr} = \frac{kT}{6\pi\eta R_h} \quad (4)$$

Where k is the Bolztmann constant, T is the temperature ($T = 296 \pm 0.5$ K), and η is the solvent viscosity. The effect of BSA on the viscosity of the solution was considered using a linear approximation based on the intrinsic viscosity of the protein provided by the manufacturer, $[\eta] = 4.13\ \text{cm}^3\ \text{g}^{-1}$. The procedure to calibrate r_0 and how it affects the experimental error in our correlation spectroscopy experiments can be found in the supporting information (Figure S3).

The minimum and maximum lag times were set to $\tau_{min} = 10\ \mu\text{s}$ and $\tau_{max} = 40$ s, respectively. This ensured reproducibility and accuracy in the analysis for all AuNP sizes studied here, according to the guidelines for correlation spectroscopy published previously.[45] We further tested that the value chosen for τ_{max} was indeed adequate for the AuNP concentrations used. Figure S5A and Table S2 show the experimental R_h for 51 nm AuNPs as a function of τ_{max} for a constant total collection time of 300 s. R_h converges to the value expected from TEM imaging (horizontal dashed line) for $\tau_{max} = 20$ s. 40 s intensity transients therefore gave correct values for R_h. In fact, for picomolar AuNP concentrations a single 40 s transients contained enough events to accurately determine R_h. This is illustrated in Figure S5B, which shows the experimental R_h retrieved from 40 s intensity transients as a function AuNP concentration expressed in terms of number of events N_{events}. The minimum number of events required per individual transient was ~ 20 for the 51 nm AuNPs. If N_{events} was less than this value, R_h was severely underestimated when compared to the size distribution obtained via TEM (red dashed lines). To avoid this artifact, the AuNP concentration was always kept in the picomolar regime, which guaranteed that at least 100 events were sampled per 40 s transients.

3. Results and Discussion

Citrate-stabilized AuNPs interacted with BSA, the most abundant protein in the circulatory system, at concentrations similar to those found for albumin in human blood (~ 0.75 mM). The normalized UV/Vis extinction spectrum of 51 nm citrate-stabilized AuNPs in Figure 1B (solid blue line) shows a strong surface plasmon resonance peak at 534 nm. The plasmon resonance maximum red-shifted by ~ 3 nm after the AuNPs were mixed with a 0.75 mM BSA solution (dashed red line). Similarly, the UV/Vis extinction spectra of citrate-stabilized 70 and 93 nm AuNPs red-shifted by 2 ~ 3 nm in the presence of BSA, as shown in Figures S2A and S2B, respectively. This suggests that BSA interacted with citrate-stabilized AuNPs and caused a change in the refractive index at the AuNP surface and consequently a shift of the plasmon resonance energy. To establish that BSA indeed binds to citrate-stabilized AuNPs, quantify the amount of adsorbed protein, and to check if protein adsorption leads to AuNP aggregation we performed *in situ* equilibrium binding experiments using scattering correlation spectroscopy in combination with analysis of the intensity transients by BIFA.

The characteristic diffusion time of AuNPs increased in the presence of BSA. Figure 2A shows the average of 56 autocorrelation curves ($\tau_{max} = 40$ s each) of 51 nm AuNPs before and after mixing with BSA at physiological concentrations. By combining equations (3) and (4), the increase in τ_D can be related to the change in R_h, which is found to be $\Delta R_h = 4.6 \pm$

1.9 nm (Figure 2A inset; see the supporting information for the calculation of the experimental error). Because BSA in its native (N) state can be approximated as a triangular equilateral prism with sides of 8 × 8 nm^2 and a height of 3.4 nm,[27] the increase in R_h corresponds to no more than monolayer adsorption of BSA bound to the AuNP surface with the triangular base. This is consistent with previous experiments investigating the adsorption of human (and bovine) serum albumin on the surfaces of AuNPs[19,31] and semiconductor nanoparticles.[18] The small discrepancy between the change in R_h and the BSA dimensions reported by x-ray crystallography[27] could be due to a solvent hydration shell and the heterogeneous AuNP size distribution.

BSA adsorption was independent of AuNP size as illustrated in Figures 2B and 2C, which show the same monolayer adsorption for 70 and 93 nm AuNPs, respectively. The characteristic diffusion times and diffusion constants for all three AuNPs samples with and without BSA as measured via scattering correlation spectroscopy are summarized in Table 1. The hydrodynamic radii R_h are also given. The values for the AuNP-BSA system were corrected for the change in viscosity when adding the BSA solution. Ignoring the contribution of the citrate capping layer, the sizes obtained by scattering correlation spectroscopy are in excellent agreement with those measured by TEM.

It is important to establish whether the change in R_h is indeed due to BSA adsorption or because of the formation of a small number of aggregates. Correlation spectroscopy is in principle an ensemble measurement technique and therefore it is difficult to exclude based on only the autocorrelation curves in Figure 2 that the increase in diffusion times was caused by the presence of a few larger AuNP aggregates instead of the formation of a BSA monolayer.[18] The fact that the change in R_h is the same for all three samples suggests that aggregation is not a dominant factor though. To further verify this, we analyzed the individual 40 s intensity transients by autocorrelation analysis independently instead of averaging them together as was done for Figure 2, because the formation of rare, large aggregates would cause a broad distribution of R_h values. This allowed us to access the distribution of R_h and analyze any changes in size heterogeneities associated with protein binding. The resulting histograms for R_h without and with BSA are shown in Figures 3A and 3B for the 51 nm AuNPs, respectively. The distribution of R_h from 56 individual 40 s intensity transients for the AuNPs only (Figure 3A) shows a Gaussian profile consistent with the size distribution observed via TEM and lacks a trailing tail of large R_h values that would be expected if aggregates were present. Figure S6 confirms that this is also the case for the R_h distribution of 70 and 93 nm AuNPs. More details regarding the analysis and an autocorrelation of a representative 40 s intensity trace (Figure S7) can be found in the supporting information.

Further evidence for the absence of AuNP aggregation and the formation of a BSA monolayer on citrate-stabilized AuNPs under physiological conditions was obtained by BIFA of individual events in the intensity transients (Figure 4). The number of events N_{events} counted per 40 s intensity transient, a good estimate of the average number of AuNPs sampled, is nearly identical for the AuNP and AuNP-BSA samples. Figure 4A shows an intensity histogram of individual bursts for the representative time transient given in the inset. The corresponding data for 51 nm AuNPs after addition of BSA is given in Figure 4B. No significant reduction in the number of events was observed. In addition, because the scattering intensity scales as $\sim d^6$ for AuNPs with diameters $d < 100$ nm,[46,47] the presence of aggregates with significantly larger scattering intensities would be evident in the intensity distribution. However, neither a decrease in the number of events nor a change in the intensity histograms towards higher values was observed, confirming that the stability of the colloid is preserved after protein adsorption. This is also the case for the 70 and 93 nm AuNPs samples, as shown in Figure 4C, where the average number $\langle N_{events} \rangle$ of events per

40 seconds is presented for at least 30 time transients per sample. The small decrease in $\langle N_{events} \rangle$ is within the experimental uncertainty and can be explained by the increase in the viscosity due to the presence of BSA. After aggregation has now been ruled out, we further quantified BSA-AuNP binding.

The adsorption isotherm for 51 nm AuNPs was found to follow an anti-cooperative binding model reaching saturation at physiological concentrations. This was achieved by constructing an adsorption isotherm over a wide range of BSA concentrations. Figure 5 shows the experimental R_h as a function of BSA concentration (red squares). Following the approach by Rocker *et al.*[18] for adsorption of human serum albumin on smaller FePt and CdSe/ZnS nanoparticles, the experimental data is fitted to a modified Langmuir model given in equation (5):

$$R_h([BSA]) = R_h(0) \sqrt[3]{1 + \frac{V_{BSA}}{V_{NP}} \frac{N}{1 + \left(\frac{K_D}{[BSA]}\right)^n}} \quad (5)$$

Here V_{BSA} and V_{NP} are the volumes of the BSA and the AuNP, respectively, N is the number of proteins bound, K_D is the dissociation constant, and n is the Hill coefficient, which measures the cooperativity of the binding. A Hill coefficient of $n = 0.4 \pm 0.1$ and a dissociation constant of $K_D = 256 \pm 50$ μM returned the best fit (dashed blue line). A Hill coefficient smaller than 1 indicates anti-cooperative binding and implies strong repulsion between bound and free BSA molecules, that increases as more surface binding sites are filled. This furthermore predicts that adsorption beyond a monolayer is negligible, in agreement with the results in Figure 2. For comparison, the traditional Langmuir model with $n = 1$ is based on the assumption that binding occurs independent of surface coverage and results in a steeper increase of R_h as a function of BSA concentration, as illustrated by the dashed black line in Figure 5. The dissociation constant corresponding to the Langmuir model is therefore an order of magnitude lower ($K_D = 20 \pm 10$ μM). While a Langmuir adsorption isotherm was reported for BSA binding to citrate-capped gold films,[38] more recent studies on nanoparticles also show an anti-cooperative binding model.[18,20,24] This difference between a nanoparticle and a film surface is presumably due to the limited number of binding sites and the surface curvature for a nanoparticle.

Knowing both n and K_D from the measured isotherm we can extract further information for BSA binding to AuNPs. First, the fit with $n = 0.4 \pm 0.1$ yields $N = 295 \pm 30$ proteins bound to the surface of the 51 nm AuNPs. The theoretically available number of binding sites for a monolayer coverage on a 51 nm AuNP is estimated to be ~ 250 by dividing the surface area of the AuNP ($S = 4 * \pi * 25.5\ nm^2 = 8171.3\ nm^2$) by the triangular cross section of the folded BSA ($1/2 * 8 * 8\ nm^2 = 32\ nm^2$). This excellent agreement gives additional confirmation for the adsorption of a monolayer of BSA in its native (N) state on citrate-capped AuNPs. Denaturation from the N-state to a partially unfolded (F) state (N-F transition)[48] after adsorption cannot be ruled out though, but all of our experiments suggest that spreading of BSA on the surface of the AuNPs is unlikely, in agreement with previous studies on AuNPs and semiconductor nanoparticles.[18,19,24,31] Second, using K_D we can also calculate the free energy of adsorption ΔG_0 according to:[49]

$$\Delta G_0 = -RT \ln(K) \quad (6)$$

where R is the gas constant and K is the binding constant, which is obtained as the inverse of K_D. Equation 6 yields $\Delta G_0 = -4.9$ kcal/mol for the anti-cooperative binding model, indicating a spontaneous process for the binding of BSA to the AuNPs.

Finally, we investigated PEG-coated AuNPs as PEG has been commonly used to prevent protein adsorption to surfaces.[50,51] We indeed found no significantly adsorption of BSA on PEG-coated AuNPs. Figure 6A shows UV/Vis extinction spectra of 56 nm PEG-functionalized AuNPs before and after addition of BSA under the same experimental conditions as for the citrate-stabilized AuNPs. No shift in the plasmon resonance maximum was observed, in contrast to the citrate-stabilized AuNPs. The autocorrelation curves presented in Figure 6B also did not show an increase in the characteristic diffusion time, and therefore the relative change in the AuNP R_h due to BSA adsorption is negligible. A protein monolayer therefore did not form on top of the PEG-coated AuNPs.

However, we cannot rule out sub-monolayer formation due to electrostatic interactions, hydrophobicity, or van der Waals forces of a few BSA molecules with the PEG-coated AuNPs. Future experiments will test this scenario, with fluorescence correlation spectroscopy using dye-labeled BSA.

BSA is a globular protein and consists of 583 amino acids, 60 of which are lysine residues, 17 disulphide bridges, a single tryptophan, and a free thiol (cysteine-34).[27] It has been proposed that BSA adsorption on citrate-capped gold surfaces could be either due to an electrostatic attraction with the positively charged lysine residues,[19,38] or by a thiol ligand displacement reaction through the unpaired cysteine.[31] In particular, Brewer *et al.* compared BSA adsorption on bare and citrate- coated flat gold surfaces using a quartz crystal microbalance and interpreted the higher binding constant for citrate-coated surfaces as an electrostatic attraction mechanism.[38] Casals *et al.* reached the same conclusion based on the observation that for small 4 nm negatively charged AuNPs formation of a protein corona was slow, which they argued was inconsistent with a ligand replacement reaction because smaller nanoparticles should have better access to the exposed thiol.[19] In contrast, Tsai *et al.* suggest a ligand exchange reaction on citrate-stabilized AuNPs via the thiol-terminated cysteine residue based on the binding constants obtained from adsorption isotherms.[31]

Because of the small size of the citrate molecules it is not possible to distinguish between ligand replacement and binding on top of the citrate stabilizing layer by correlation spectroscopy. We also measured the zeta potential of the citrate-capped AuNPs before and after addition of BSA. Figure S8 shows that the surface potential of the AuNPs became less negative due to BSA adsorption, consistent with an electrostatic binding mechanism via the positively charged lysine residues. However, replacing the negatively charged citrate molecules with BSA is expected to have a similar effect because BSA is also overall negatively charged at physiological pH.[40] Furthermore, we note that many surface functionalization procedures of the same citrate-capped AuNPs involve the initial replacement of the citrate, which is used for the AuNP growth, with especially sulfur terminated ligands.[52] In the case of the PEG-coated AuNPs, the zeta potential measurements showed that the AuNPs are only slightly negatively charged (Figure S8). Following the electrostatic binding mechanism, this reduction in surface charge could therefore explain the absence of BSA adsorption. It should be pointed out though that because the length of the PEG molecules is about 5 nm for a fully stretched conformation and therefore comparable with the height of the BSA, the correlation spectroscopy measurements presented here make it difficult to distinguish between no BSA adsorption and a thiol-thiol exchange reaction. However, as the PEG is also bound via a sulfur group to the AuNP surface the latter scenario is rather unlikely as the free energy for the replacement of one thiol with another one has been determined to be $\Delta G_0 \sim +30$ kcal/mol in the case of self-assembled

monolayers on flat gold surfaces.[53] Further experiments with different surface charges and chemistries are planned to obtain a more complete picture and to establish the role of different adsorption mechanisms with distinct effects on the biological activity. Significant more insight into the adsorption mechanism at the nano-bio interface can be obtained by labeling the protein and possibly the ligands with dye molecules and performing multi-color (excitation and detection) auto- and cross-correlation spectroscopy.

4. Conclusions

We have shown *in situ* evidence for adsorption of BSA on citrate-stabilized AuNPs. UV/Vis extinction spectroscopy revealed a red-shift in the surface plasmon resonance for the citrate-stabilized AuNPs. Quantitative analysis of the diffusion parameters before and after protein adsorption showed an increase in the AuNP hydrodynamic radius. The change in hydrodynamic radius corresponds to the formation of a BSA monolayer independent of AuNP size for diameters ranging between 51 and 93 nm. Combining correlation spectroscopy with BIFA, we furthermore demonstrated that protein adsorption does not lead to AuNP aggregation. An adsorption isotherm showed that the association of BSA to citrate-stabilized AuNPs can be described by an anti-cooperative binding model, which yielded a number of bound protein molecules in agreement with the estimated number of binding sites based on the equilateral base of N-state BSA and the AuNP surface area. These results are in good agreement with previous *in situ* measurements of smaller 10 nm citrate-stabilized AuNPs interacting with BSA, studied by dynamic light scattering.[19] Furthermore, we demonstrated that BSA adsorption is negligible on PEG-coated AuNPs. Although the system studied here was specific - BSA interacting with citrate-stabilized AuNPs, the *in situ* approach using correlation spectroscopy and BIFA presented here can be directly applied to other nanoparticle-protein interactions.

Supplementary Material

Refer to Web version on PubMed Central for supplementary material.

Acknowledgments

S.L. acknowledges support from the Robert A. Welch Foundation [Grant C-1664] and the Cancer Prevention and Research Institute of Texas [CPRIT RP110355]. C.F.L. thanks the Norman Hackerman Welch Young Investigator Program at Rice University, the National Science Foundation [Grants CBET-1134417 and CHE-1151647], and the National Institutes of Health [Grant GM94246-01A1]. P.S. acknowledges support from the Royal Thai Government. We thank Dr. Alexei Tcherniak and Dr. Wei-Shun Chang for insightful discussions and Dr. Nitesh Poddar for assistance with the preparation of the PEG-functionalized microscope coverslips.

References

1. Nel AE, Madler L, Velegol D, Xia T, Hoek EMV, Somasundaran P, Klaessig F, Castranova V, Thompson M. Understanding biophysicochemical interactions at the nano-bio interface. Nature Mater. 2009; 8:543–557. [PubMed: 19525947]
2. Xia XR, Monteiro-Riviere NA, Riviere JE. An index for characterization of nanomaterials in biological systems. Nat Nanotech. 2010; 5:671–675.
3. Moyano DF, Rotello VM. Nano meets biology: Structure and function at the nanoparticle interface. Langmuir. 2011; 27:10376–10385. [PubMed: 21476507]
4. Wang B, Zhang L, Bae SC, Granick S. Nanoparticle-induced surface reconstruction of phospholipid membranes. Proc Nat Acad Sci US A. 2008; 105:18171–18175.
5. Zhang D, Neumann O, Wang H, Yuwono VM, Barhoumi A, Perham M, Hartgerink JD, Wittung-Stafshede P, Halas NJ. Gold nanoparticles can induce the formation of protein-based aggregates at physiological pH. Nano Lett. 2009; 9:666–671. [PubMed: 19199758]

6. Mahmoudi M, Lynch I, Ejtehadi MR, Monopoli MP, Bombelli FB, Laurent S. Protein-nanoparticle interactions: Opportunities and challenges. Chem Rev. 2011; 111:5610–5637. [PubMed: 21688848]
7. De M, Rana S, Akpinar H, Miranda OR, Arvizo RR, Bunz UHF, Rotello VM. Sensing of proteins in human serum using conjugates of nanoparticles and green fluorescent protein. Nature Chem. 2009; 1:461–465. [PubMed: 20161380]
8. Dobrovolskaia MA, Patri AK, Zheng J, Clogston JD, Ayub N, Aggarwal P, Neun BW, Hall JB, McNeil SE. Interaction of colloidal gold nanoparticles with human blood: Effects on particle size and analysis of plasma protein binding profiles. Nanomedicine. 2009; 5:106–117. [PubMed: 19071065]
9. Clift MJD, Bhattacharjee S, Brown DM, Stone V. The effects of serum on the toxicity of manufactured nanoparticles. Toxicol Lett. 2010; 198:358–365. [PubMed: 20705123]
10. Cheng Y, Samia AC, Li J, Kenney ME, Resnick A, Burda C. Delivery and efficacy of a cancer drug as a function of the bond to the gold nanoparticle surface. Langmuir. 2010; 26:2248–2255. [PubMed: 19719162]
11. Hu CMJ, Zhang L, Aryal S, Cheung C, Fang RH, Zhang L. Erythrocyte membrane-camouflaged polymeric nanoparticles as a biomimetic delivery platform. Proc Nat Acad Sci US A. 2011; 108:10980–10985.
12. Huschka R, Zuloaga J, Knight MW, Brown LV, Nordlander P, Halas NJ. Light-Induced Release of DNA from Gold Nanoparticles: Nanoshells and Nanorods. J Am Chem Soc. 2011; 133:12247–12255. [PubMed: 21736347]
13. Pissuwan D, Valenzuela SM, Cortie MB. Therapeutic possibilities of plasmonically heated gold nanoparticles. Trends Biotechnol. 2006; 24:62–67. [PubMed: 16380179]
14. Zharov VP, Mercer KE, Galitovskaya EN, Smeltzer MS. Photothermal nanotherapeutics and nanodiagnostics for selective killing of bacteria targeted with gold nanoparticles. Biophys J. 2006; 90:619–627. [PubMed: 16239330]
15. Kim JW, Galanzha EI, Shashkov EV, Moon HM, Zharov VP. Golden carbon nanotubes as multimodal photoacoustic and photothermal high-contrast molecular agents. Nat Nanotech. 2009; 4:688–694.
16. Cho EC, Glaus C, Chen J, Welch MJ, Xia Y. Inorganic nanoparticle-based contrast agents for molecular imaging. Trends Mol Med. 2010; 16:561–573. [PubMed: 21074494]
17. Gobin AM, Watkins EM, Quevedo E, Colvin VL, West JL. Near-infrared resonant gold/gold sulfide nanoparticles as a photothermal cancer therapeutic agent. Small. 2010; 6:745–752. [PubMed: 20183810]
18. Rocker C, Potzl M, Zhang F, Parak WJ, Nienhaus GU. A quantitative fluorescence study of protein monolayer formation on colloidal nanoparticles. Nat Nanotech. 2009; 4:577–580.
19. Casals E, Pfaller T, Duschl A, Oostingh GJ, Puntes V. Time evolution of the nanoparticle protein corona. ACS Nano. 2010; 4:3623–3632. [PubMed: 20553005]
20. Lacerda SHDP, Park JJ, Meuse C, Pristinski D, Becker ML, Karim A, Douglas JF. Interaction of gold nanoparticles with common human blood proteins. ACS Nano. 2010; 4:365–379. [PubMed: 20020753]
21. Walkey CD, Chan WCW. Understanding and controlling the interaction of nanomaterials with proteins in a physiological environment. Chem Soc Rev. 2012; 41:2780–2799. [PubMed: 22086677]
22. Lundqvist M, Stigler J, Elia G, Lynch I, Cedervall T, Dawson KA. Nanoparticle size and surface properties determine the protein corona with possible implications for biological impacts. Proc Nat Acad Sci US A. 2008; 105:14265–14270.
23. Tenzer S, Docter D, Rosfa S, Wlodarski A, Kuharev J, Rekik A, Knauer SK, Bantz C, Nawroth T, Bier C, et al. Nanoparticle size is a critical physicochemical determinant of the human blood plasma corona: A comprehensive quantitative proteomic analysis. ACS Nano. 2011; 5:7155–7167. [PubMed: 21866933]
24. Chakraborty S, Joshi P, Shanker V, Ansari ZA, Singh SP, Chakrabarti P. Contrasting effect of gold nanoparticles and nanorods with different surface modifications on the structure and activity of bovine serum albumin. Langmuir. 2011; 27:7722–7731. [PubMed: 21591651]

25. Dutta D, Sundaram SK, Teeguarden JG, Riley BJ, Fifield LS, Jacobs JM, Addleman SR, Kaysen GA, Moudgil BM, Weber TJ. Adsorbed proteins influence the biological activity and molecular targeting of nanomaterials. Toxicol Sci. 2007; 100:303–315. [PubMed: 17709331]
26. Doorley GW, Payne CK. Cellular binding of nanoparticles in the presence of serum proteins. Chem Commun. 2011; 47:466–468.
27. He XM, Carter DC. Atomic structure and chemistry of human serum albumin. Nature. 1992; 358:209–215. [PubMed: 1630489]
28. Deng ZJ, Liang M, Monteiro M, Toth I, Minchin RF. Nanoparticle-induced unfolding of fibrinogen promotes Mac-1 receptor activation and inflammation. Nat Nanotech. 2011; 6:39–44.
29. Walczyk D, Bombelli FB, Monopoli MP, Lynch I, Dawson KA. What the cell "sees" in bionanoscience. J Am Chem Soc. 2010; 132:5761–5768. [PubMed: 20356039]
30. Cedervall T, Lynch I, Foy M, Berggard T, Donnelly SC, Cagney G, Linse S, Dawson KA. Detailed Identification of Plasma Proteins Adsorbed on Copolymer Nanoparticles13. Angew Chem Int Ed. 2007; 46:5754–5756.
31. Tsai DH, DelRio FW, Keene AM, Tyner KM, MacCuspie RI, Cho TJ, Zachariah MR, Hackley VA. Adsorption and conformation of serum albumin protein on gold nanoparticles investigated using dimensional measurements and in situ spectroscopic methods. Langmuir. 2011; 27:2464–2477.
32. Monopoli MP, Walczyk D, Campbell A, Elia G, Lynch I, Baldelli Bombelli F, Dawson KA. Physical-chemical aspects of protein corona: relevance to in vitro and in vivo biological impacts of nanoparticles. J Am Chem Soc. 2011; 133:2525–2534. [PubMed: 21288025]
33. Linse S, Cabaleiro-Lago C, Xue WF, Lynch I, Lindman S, Thulin E, Radford SE, Dawson KA. Nucleation of protein fibrillation by nanoparticles. Proc Nat Acad Sci US A. 2007; 104:8691–8696.
34. Alkilany AM, Murphy CJ. Toxicity and cellular uptake of gold nanoparticles: what we have learned so far? J Nanopart Res. 2010; 12:2313–2333. [PubMed: 21170131]
35. Link S, El-Sayed MA. Shape and size dependence of radiative, non-radiative and photothermal properties of gold nanocrystals. Int Rev Phys Chem. 2000; 19:409–453.
36. Chang WS, Ha JW, Slaughter LS, Link S. Plasmonic nanorod absorbers as orientation sensors. Proc Nat Acad Sci US A. 2010; 107:2781–2786.
37. Slaughter LS, Wu Y, Willingham BA, Nordlander P, Link S. Effects of Symmetry Breaking and Conductive Contact on the Plasmon Coupling in Gold Nanorod Dimers. ACS Nano. 2010; 4:4657–4666. [PubMed: 20614909]
38. Brewer SH, Glomm WR, Johnson MC, Knag MK, Franzen S. Probing BSA binding to citrate-coated gold nanoparticles and surfaces. Langmuir. 2005; 21:9303–9307. [PubMed: 16171365]
39. Tcherniak A, Dominguez-Medina S, Chang WS, Swanglap P, Slaughter LS, Landes CF, Link S. One-photon plasmon luminescence and its application to correlation spectroscopy as a probe for rotational and translational dynamics of gold nanorods. J Phys Chem C. 2011; 115:15938–15949.
40. Theodore, P. All about albumin: Biochemistry, genetics and medical applications. 1. Academic Press; San Diego, CA: 1996.
41. Tcherniak A, Prakash A, Mayo JT, Colvin VL, Link S. Fluorescence correlation spectroscopy of magnetite nanocrystal diffusion. J Phys Chem C. 2008; 113:844–848.
42. Daniels CR, Reznik C, Kilmer R, Felipe MJ, Tria MCR, Kourentzi K, Chen WH, Advincula RC, Willson RC, Landes CF. Permeability of anti-fouling PEGylated surfaces probed by fluorescence correlation spectroscopy. Colloids Surf B. 2011; 88:31–38.
43. Haustein E, Schwille P. Ultrasensitive investigations of biological systems by fluorescence correlation spectroscopy. Methods. 2003; 29:153–166. [PubMed: 12606221]
44. Aragon SR, Pecora R. Fluorescence correlation spectroscopy as a probe of molecular dynamics. J Chem Phys. 1976; 64:1791–1803.
45. Tcherniak A, Reznik C, Link S, Landes CF. Fluorescence correlation spectroscopy: Criteria for analysis in complex systems. Anal Chem. 2008; 81:746–754. [PubMed: 19093758]
46. Tcherniak A, Ha JW, Dominguez-Medina S, Slaughter LS, Link S. Probing a century old prediction one plasmonic particle at a time. Nano Lett. 2010; 10:1398–1404. [PubMed: 20196552]

47. Chang WS, Slaughter LS, Khanal BP, Manna P, Zubarev ER, Link S. One-Dimensional Coupling of Gold Nanoparticle Plasmons in Self-Assembled Ring Superstructures. Nano Lett. 2009; 9:1152–1157. [PubMed: 19193117]

48. Khan MY. Direct evidence for the involvement of domain III in the N-F transition of bovine seruma albumin. Biochem J. 1986; 236:307–310. [PubMed: 3790080]

49. Haber LH, Kwok SJJ, Semeraro M, Eisenthal KB. Probing the colloidal gold nanoparticle/aqueous interface with second harmonic generation. Chem Phys Lett. 2011; 507:11–14.

50. He Q, Zhang J, Shi J, Zhu Z, Zhang L, Bu W, Guo L, Chen Y. The effect of PEGylation of mesoporous silica nanoparticles on nonspecific binding of serum proteins and cellular responses. Biomaterials. 2010; 31:1085–1092. [PubMed: 19880176]

51. Pinholt C, Bukrinsky JT, Hostrup S, Frokjaer S, Norde W, Jorgensen L. Influence of PEGylation with linear and branched PEG chains on the adsorption of glucagon to hydrophobic surfaces. Eur J Pharm Biopharm. 2011; 77:139–147. [PubMed: 21074613]

52. Dreaden EC, Alkilany AM, Huang X, Murphy CJ, El-Sayed MA. The golden age: Gold nanoparticles for biomedicine. Chem Soc Rev. 2012; 41:2740–2779. [PubMed: 22109657]

53. Love JC, Estroff LA, Kriebel JK, Nuzzo RG, Whitesides GM. Self-assembled monolayers of thiolates on metals as a form of nanotechnology. Chem Rev. 2005; 105:1103–1170. [PubMed: 15826011]

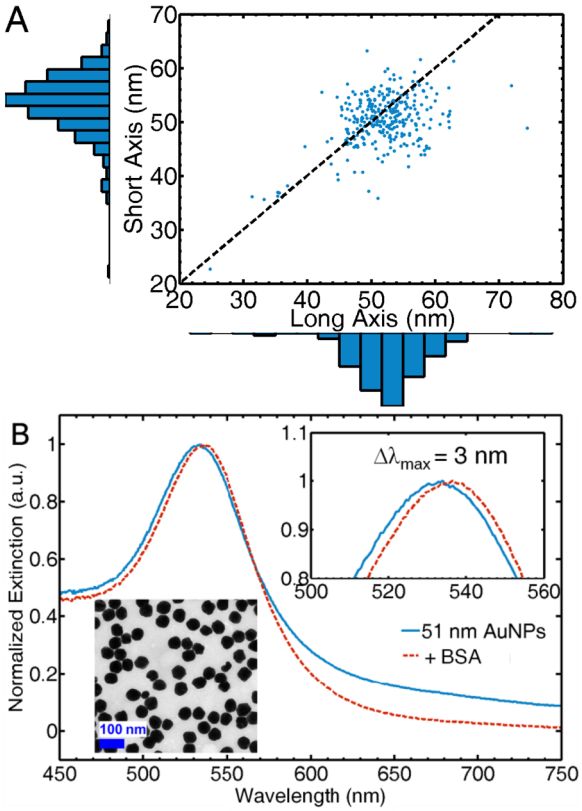

Figure 1.

(A)Size distribution of 51 nm AuNPs obtained by TEM. The dashed black line represents an aspect ratio of 1, or perfect spherical shape. (B) Normalized UV/Vis ensemble extinction spectra of 51 nm AuNPs before (solid, blue) and after (dashed, red) mixing with BSA at 0.75 mM. The lower left inset contains a representative TEM image of the sample. The upper right inset zooms into the region of the surface plasmon resonance maximum λ_{max}.

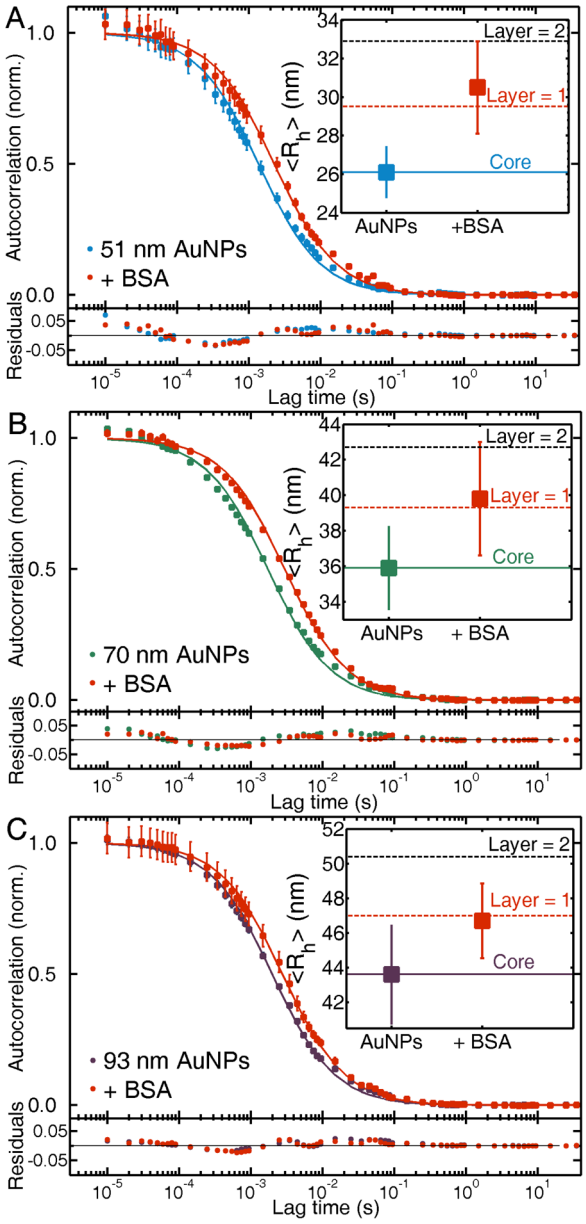

Figure 2.

Autocorrelation curves of AuNPs and AuNPs + BSA [0.75 mM], for three AuNPs samples with mean diameters of 51 nm (A), 70 nm (B) and 93 nm (C). The amplitude of the autocorrelation is normalized to 1 for better comparison of the characteristic diffusion time, τ_D. The average hydrodynamic radius $\langle R_h \rangle$ obtained from the autocorrelation curves is shown as squares in the insets. The expected increase in R_h due to BSA binding is 3.4 nm per layer (dashed lines). The error bars represent the experimental uncertainty of three to five independent measurements.

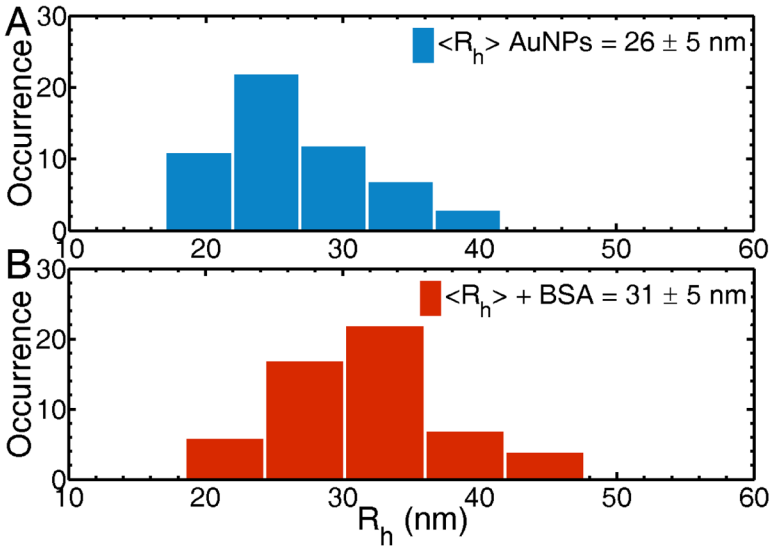

Figure 3.

Distribution of R_h obtained by autocorrelation analysis of individual 40 s intensity transients. The width of the histrogram bars corresponds to the error in R_h calculated with equation S6 for an individual transient. The error quoted in the figure is the standard deviation of the distribution.

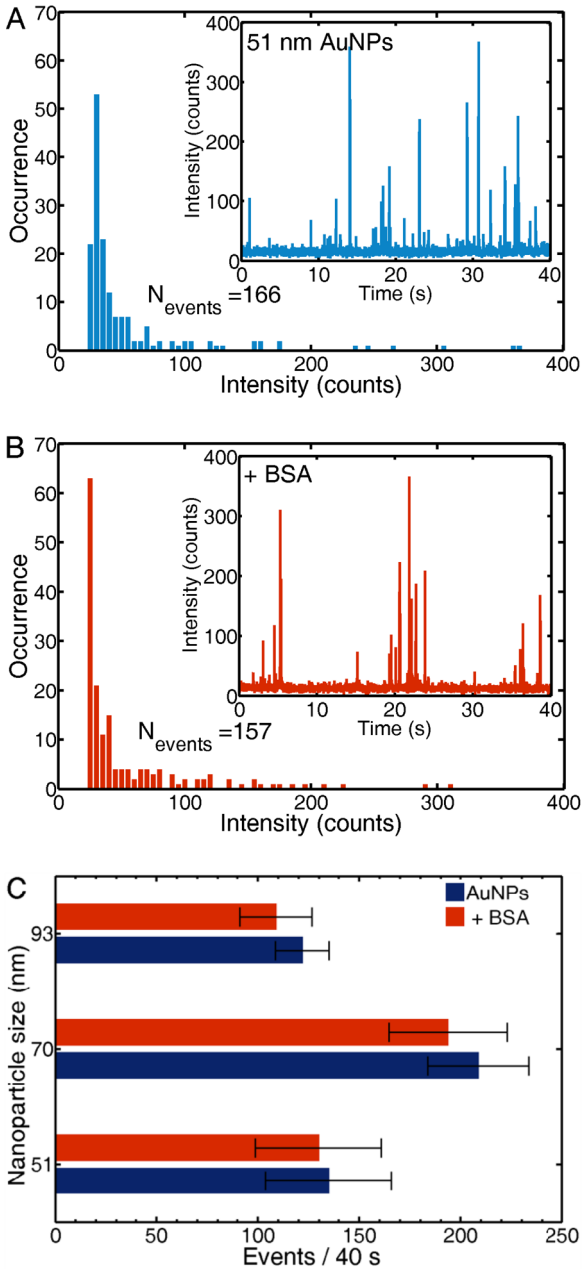

Figure 4.

Blip intensity frequency analysis (BIFA) of 51 nm AuNPs before (A) and after (B) binding to BSA [0.75 mM]. The events are counted based on 40 s intensity transients displayed in the insets. (C) Average number of events before (blue) and after (red) binding to BSA for the three AuNP sizes measured. The error bars represent one standard deviation from the average value.

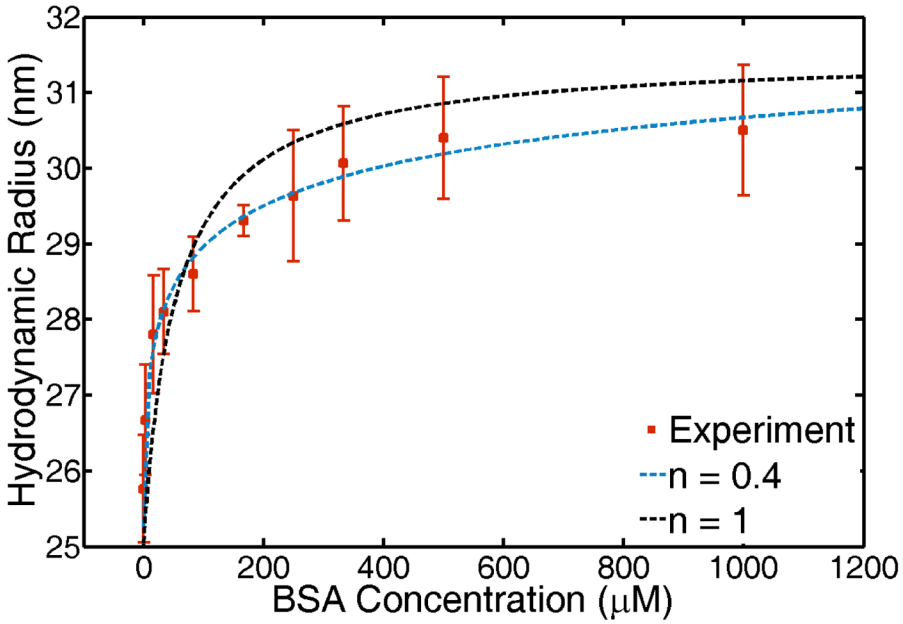

Figure 5.

Adsorption isotherm relating the concentration of BSA with the nanoparticle R_h (red squares). The data is fitted to the Langmuir model given by equation 5. A Hill coefficient n of 0.4 returns the best fit (blue line). A comparison to a non-cooperative binding model (n = 1) is shown by the black line.

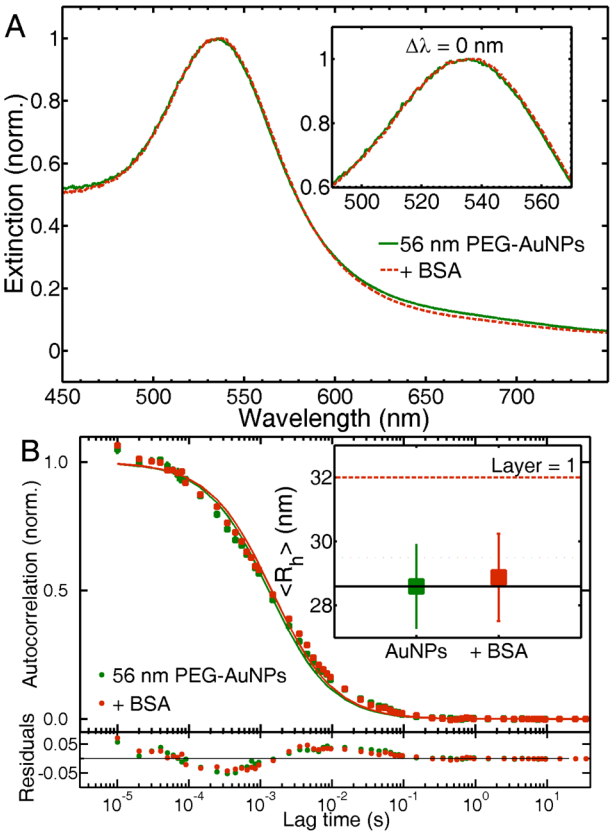

Figure 6.

(A) Normalized UV/VIS extinction spectra of 56 nm PEG-coated AuNPs before (solid green line) and after (dashed red line) addition of BSA. The inset zooms into the region of λ_{max}. (B) Autocorrelation curves of 56 nm PEG-coated AuNPs before (green) and after (red) addition of BSA. The inset shows the average hydrodynamic radius $<R_h>$ obtained from autocorrelation analysis. For comparison, the expected increase in R_h based on one layer of BSA is shown by the dashed red line.

Table 1

Characteristic diffusion time τ_D, translational diffusion coefficient D_{tr} and hydrodynamic radius R_h obtained via autocorrelation analysis of AuNPs. The size distribution obtained via TEM (R_{TEM}) is shown for comparison.

Sample	R_{TEM} [10^{-9}m]	$\tau_{D,\,AuNPs}$ [10^{-3} s]	$\tau_{D,\,+\,BSA}$ [10^{-3} s]	$D_{tr,\,AuNPs}$ [10^{-6} m^2 s^{-1}]	$D_{tr,\,+\,BSA}$ [10^{-6} m^2 s^{-1}]	$R_{h,\,AuNPs}$ [10^{-9}m]	$R_{h,\,+\,BSA}$ [10^{-9}m]
51 nm	25.6 ± 3.4	1.7 ± 0.3	2.9 ± 0.5	9.3 ± 0.5	6.1 ± 0.4	26.0 ± 1.3	30.6 ± 2.4
70 nm	35.1 ± 4.3	2.1 ± 0.1	3.0 ± 0.3	7.2 ± 0.5	4.7 ± 0.4	35.9 ± 2.3	39.8 ± 3.2
93 nm	46.6 ± 3.3	2.5 ± 0.3	3.2 ± 0.2	5.6 ± 0.4	4.3 ± 0.2	43.6 ± 2.8	47.7 ± 2.2
56 nm PEG	27.9 ± 3.3	2.1 ± 0.4	2.4 ± 0.5	8.5 ± 0.4	6.9 ± 0.4	28.6 ± 1.3	28.9 ± 1.4